Desalination and Water Treatment
www.deswater.com

doi: 10.5004/dwt.2018.21901

102 (2018) 241–252
January

Deposition of Ag nanoparticles onto TiO_2/Fe_3O_4/MWCNTs quaternary nanocomposite: a visible-light-driven plasmonic photocatalyst for degradation of 2,4-dichlorophenol

Sara Pakdaman, Azadeh Ebrahimian Pirbazari*, Neda Gilani

Fouman Faculty of Engineering, College of Engineering, University of Tehran, P.O. Box 43515-1155, Fouman 43516-66456, Iran, Tel. +981334734927; Fax: +981334737228; emails: aebrahimian@ut.ac.ir (A.E. Pirbazari), sara.pakdamaan@gamil.com (S. Pakdaman), gilani@ut.ac.ir (N. Gilani)

Received 31 July 2017; Accepted 4 January 2018

ABSTRACT

In this research, we developed a facile method to synthesize novel quaternary plasmonic photocatalysts TiO_2/Fe_3O_4/MWCNTs/Ag (TFC-Ag samples) containing different amounts of silver. The obtained samples were evaluated by different analyses such as X-ray diffraction, scanning electron microscopy/energy dispersive X-ray spectroscopy, UV–Vis diffuse reflectance spectroscopy, N_2 physisorption, vibrating sample magnetometer, and transmission electron microscopy. The prepared samples exhibit a high visible-light photocatalytic activity for 2,4-dichlorophenol (2,4-DCP) degradation compared with pure TiO_2 in aqueous solution. The highest photocatalytic degradation efficiency was observed for the TFC-Ag sample containing 1.79 wt% silver. In the presence of pure TiO_2 and quaternary TFC-Ag(1.79) nanocomposite, we obtained respectively 30% and 80% 2,4-DCP degradation after 180 min irradiation under visible light. The excellent visible-light photocatalytic activity of TFC-Ag samples can be attributed to the surface plasmon resonance effect of Ag nanoparticles anchored on TiO_2 and charge separation by MWCNTs. It was found that the degradation reactions follow the first-order kinetics. Reusing experiments of the best photocatalyst (TFC-Ag(1.79)) did not show any reduction under visible light in catalyst activity for 2,4-DCP degradation after four cycles.

Keywords: Ag nanoparticles; Quaternary nanocomposite; MWCNTs; Degradation; Plasmonic resonance

1. Introduction

Visible-light-driven photocatalysis has received a growing attention over the past decades for degradation of pollutants because it can directly use the sunlight to deal with environmental problems [1]. In modern countries, semiconductor-based photocatalysts have been received much attention for organic and inorganic pollutants photocatalytic degradation and alteration of solar energy. Among various semiconductors, TiO_2 is recognized as the most promising semiconductor owing to its biological and chemical inactivity, high oxidizing influence, low cost, long-term stability, and environmentally friendly [2–6]. The limited UV-induced activity of TiO_2 due to its wide band gap (i.e., 3.2 eV for anatase and 3.0 eV for rutile) has considerably prevented its environmental application under visible light. Moreover, low surface area and slow transfer rate of charge carriers also hinder the photocatalyst expansion. These conditions encourage scholars to develop new photocatalysts with desirable photocatalytic performance under visible light. To overcome the existing drawbacks, numerous methods have been used to extend TiO_2 semiconductor absorption spectrum into the visible region; e.g., nonmetal doping [7–9], metal deposition [10–12], and coupling with other semiconductors [13–15]. Among these methods, the use of noble metal nanoparticles (NPs) has obtained more attention due to the surface plasmon resonance (SPR) of NPs, which accelerates the separation of photogenerated electrons and holes on the catalyst's

* Corresponding author.

surface. Moreover, Ag NPs loaded on semiconductors are believed to show efficient plasmon resonance under visible light [16–18]. Plasmonic photocatalysts act as photosensitizers and have two unique features, SPR and Schottky junction. Schottky junction results from metal–semiconductor contact generate an internal electric field that reduces the recombination of charge carriers. In addition, SPR properties of noble metal NPs enhance the local electric field, leading to strong SPR absorption of visible light [19–21]. Coupling of TiO_2 with Ag NPs is a promising method for efficient degradation of pollutants into the visible region. Moreover, the coupling of carbonaceous materials, such as carbon nanotubes, graphene, carbon sphere with TiO_2 semiconductor has been shown to improve the photoactivity performance by reducing the rapid recombination rate of electron–hole pairs [22–24]. Recently, multi-walled carbon nanotubes (MWCNTs) have attracted significant attention in the area of photocatalysis because of their large surface area, excellent physical and chemical properties, and one-dimensional structure. MWCNTs enhance the photoactivity performance according to two major factors: (1) they facilitate electron transfer because of their high electrical conductivity and (2) they act as an electron reservoir and reduce the charge carriers' recombination [25]. MWCNTs in MWCNTS/TiO_2 composite act as a dispersing agent that can control the morphology and the crystal size of TiO_2. Also, they act as adsorbent and photosensitizer that enhance the photoactivity performance of TiO_2 in the visible region [25,26]. The synergetic effect of Ag,TiO_2, and MWCNTs for enhancing the visible light photoactivity performance is a new way to develop efficient visible-light-driven photocatalysts. MWCNTs/TiO_2 hybrids suffer from difficult recollection for environmental applications. Compared with the conventional separation techniques such as filtration and centrifugation, magnetically separation using an external magnetic field is an efficient method for collecting nanosized photocatalysts and reducing the loss of photocatalyst materials during the separation process [27–32].

In the present work, we report the synthesis of quaternary TiO_2/Fe_3O_4/MWCNTs/Ag nanocomposites containing different quantities of silver. Structural and morphological properties of the obtained samples were investigated by different analyses including X-ray diffraction (XRD), scanning electron microscope (SEM)/energy dispersive X-ray (EDX), diffuse reflectance spectroscopy (DRS), N_2 physisorption, vibrating sample magnetometer (VSM) and transmission electron microscopy (TEM) techniques. By employing the photocatalytic degradation of 2,4-dichlorophenol (2,4-DCP) as a model reaction, we investigated the photoactivity the obtained nanocomposites efficiency. Chlorophenols are toxic chemicals that are used in many industrial applications such as petrochemicals, pesticide, dye intermediates, and paint [33]. Especially, 2,4-DCP is an important chemical precursor for the manufacture of a widely used herbicide, 2,4-dichlorophenoxy acetic acid [34]. However, 2,4-DCP may cause some pathological symptoms and change human endocrine systems. Their mode of exposure is through the skin and gastrointestinal tract. In recent years, concerns have been raised about chlorophenols' persistence and bioaccumulation both in animals and in humans [35–37]. So, it would be crucial to seek innovative and effective ways to minimize the harm of chlorophenols in the environment. To the best of our knowledge, this is the first study on the preparation and visible-light photocatalytic activity of plasmonic photocatalyst TiO_2/Fe_3O_4/MWCNTs/Ag nanocomposite prepared by sol–gel method. The outstanding properties associated with the nanocomposites suggested that they can be applied as a novel visible light harvesting catalyst for given applications in photocatalysis. The quaternary nanocomposites exhibited an improved efficiency for 2,4-DCP photocatalytic degradation.

2. Experimental

2.1. Materials

MWCNTs functionalized by carboxylic groups were obtained from Neutrino Corporation (Iran). The average diameter and length of MWCNTs were 10–20 nm × 0.5–2 μm, respectively. $FeCl_3{\cdot}6H_2O$ (Merck, No. 103943), $FeSO_4{\cdot}7H_2O$ (Merck, No. 103965) were used for the synthesis of Fe_3O_4 NPs. Tetraisopropylorthotitanat (TIP; Merck (Germany), No. 8.21895), anhydrous ethanol, ammonia, and high-purity 2,4-DCP, 98% (Merck, No. 803774) were used as probe molecules for photocatalytic experiments. Silver nitrate ($AgNO_3$), 99.9%, was obtained by (Merck, No. 101510). All the reagents were of analytical grade and applied without additional purification. For the preparation of all aqueous solutions, double distilled water was applied.

2.2. Preparation of Fe_3O_4 NPs

We synthesized Fe_3O_4 NPs through chemical precipitation technique under an inert atmosphere (nitrogen 99.999%) and alkaline conditions [38].

2.3. Preparation of TiO_2/Fe_3O_4/MWCNTs samples

To prepare TiO_2/Fe_3O_4/MWCNTs samples, 0.1 g Fe_3O_4 NPs was prepared according to the procedure described in section 2.2. Then, 4 mL TIP was mixed with 70 mL anhydrous ethanol and was ultrasonicated (Elma, Germany, E60H, ultrasound bath) for 1 h. Next, 0.06 g of functionalized MWCNTs was added to form solution A, which was ultrasonicated for further 3 h. Solution B was prepared by diluting 3 mL acetic acid in 90 mL deionized water. Solution B was added drop wise into solution A at 50°C through mechanical stirring. Subsequently, the resulting solution was stirred for 30 min. Finally, after cooling to room temperature, the solid product from the suspension was separated by employing a magnet and washed with water and ethanol for several times and then dried in a vacuum for 12 h at 60°C. The resulting powder was annealed at 300°C for 1 h to produce TiO_2/Fe_3O_4/MWCNTs nanocomposite. From now on, these samples will be shown as TFC. Also, pure TiO_2 in the same route was synthesized for control experiments.

2.4. Ag loading onto TiO_2/Fe_3O_4/MWCNTs sample

The prepared TFC sample (section 2.3) was decorated with Ag NPs according to the procedure described by Huerta Aguilar et al. [39]. For this purpose, 0.5 g of TFC was suspended by sonication in 10 mL of deionized water to which $AgNO_3$ (0.5, 1.0, and 1.5 mL, 100.0 mM) was added slowly; the resulting

solution was stirring at 20°C for 30 min and then Na_2CO_3 (0.5 mL, 1.0% w/v) was added slowly. The resulting slurry was separated by filtering and dried at room temperature. These quaternary nanocomposites were labeled as TFC-Ag(a), where (a) is the quantity of silver estimated by EDX analysis.

2.5. Characterization

XRD patterns were recorded using a Siemens, D5000 (Germany) apparatus. The diffractograms were recorded using Cu K_α radiation as the X-ray source in the 2θ range of 20°–80°. The morphology of the obtained samples was identified using SEM (Vegall-Tescan Company, Brno, Czech Republic) equipped with an EDX. The samples UV–Vis DRS were recorded by an Ava Spec-2048TEC spectrometer. The prepared samples microstructure and morphology were investigated by TEM (Philips CM30 300 kV). The nitrogen physisorption measurements were performed with a Quantachrome Autosorb-1-MP (Micromeritics, Germany). The Brunauer–Emmett–Teller (BET) areas were determined by static nitrogen physisorption at –196°C followed by out-gassing at 200°C until the pressure was lower than 5 mbar. VSM (The system is made of Meghnatis Daghighe Kavir (MDK) Company, Kashan I. R., Iran).

2.6. 2,4-DCP photocatalytic degradation

We selected 2,4-DCP as an organic pollutant model to investigate the photocatalytic efficiency of the obtained samples. We used two kinds of irradiation source with illumination power within the UV and visible region. For UV region experiments, we used 400 W Kr lamp (Osram, Germany), with 90% illumination power in the UV-A region (400–315 nm) and about 10% in the UV-B region (315–280 nm). For visible light experiments, we used a halogen lamp (ECO OSRAM, 500W, 350–800 nm) with the main peak at 575 nm. In each photocatalytic degradation experiment, the baker containing 10 mg photocatalyst and 100 mL 2,4-DCP aqueous solution (40 mg/L) in the dark was stirred first for 10 min for desorption/adsorption equilibrium, followed by turning the lamp on for 180 min. At certain times, 2 mL of solution was withdrawn and filtered to eliminate the photocatalyst and analyze it using Rayleigh UV-2601 UV/VIS spectrophotometer (λ_{max} = 227 nm).

3. Results and discussion

3.1. X-ray diffraction analysis

Fig. 1 shows the purchased MWCNTs and the synthesized Fe_3O_4 NPs XRD patterns. Fig. 1(a) shows a broad crystalline diffraction around 25.5°, which shows the MWCNTs characteristic diffraction [40]. In XRD pattern of Fe_3O_4 NPs (Fig. 1(b)), we detected the characteristic diffractions at 2θ = 30.2°, 35.6°, 43.5°, 54.3°, 57.4°, and 63.1° that can be indexed to the reflection of cubic spinel structured of the Fe_3O_4. This result is consistent with those reported by JCPDS card number 19-0629 [41], suggesting that phase purity of Fe_3O_4 and well-resolved diffraction peaks verify high crystallinity of Fe_3O_4 NPs. Fig. 2 presents the XRD patterns of pure TiO_2, TFC, and TFC-Ag(a) samples. In XRD pattern of pure TiO_2 (Fig. 2(a)), the strong

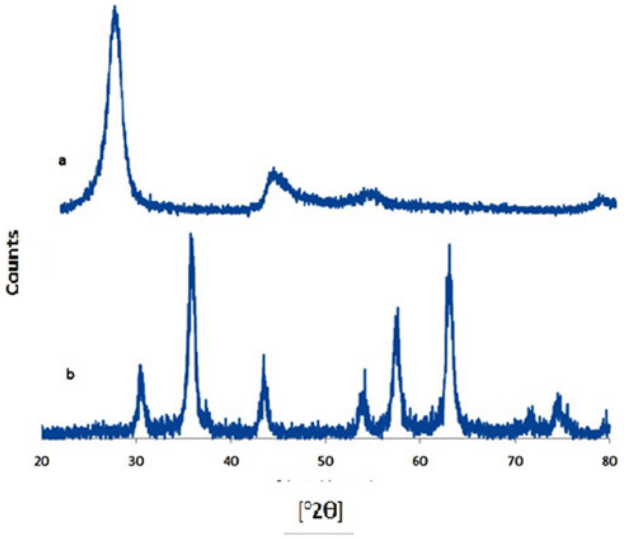

Fig. 1. XRD patterns of (a) MWCNTs and (b) Fe_3O_4 NPs.

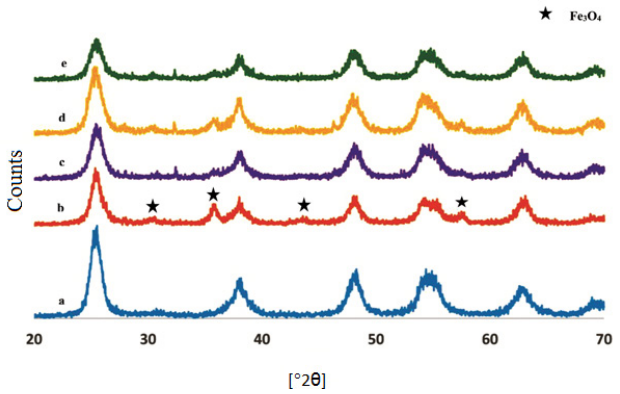

Fig. 2. XRD patterns of (a) TiO_2, (b) TFC, (c) TFC-Ag(2.58), (d) TFC-Ag(1.79), and (e) TFC-Ag(3.18).

diffractions at 2θ = 25.3°, 37.7°, 48.0°, 53.8°, 55.0°, and 62.6° confirmed pure anatase phase formation [42]. Fig. 2(b) shows TFC sample XRD pattern. The diffractions of this sample are in a good agreement with the XRD patterns of pure TiO_2 and Fe_3O_4 NPs, but the intensity of the diffractions is relatively lower compared with the pure materials. The main diffraction of MWCNTs was not observed due to the low content of MWCNTs compared with Fe_3O_4 and anatase TiO_2. In addition to diffractions of Fe_3O_4 (showed with an asterisk), there are other diffraction peaks appeared at 2θ = 25.3°, 37.7°, 48.0°, 53.8°, 55.0°, and 62.6° attributing to pure anatase TiO_2 [42]. Figs. 2(c)–2(e) show the XRD patterns of TFC-Ag(a) samples. Four peaks at 2θ values of 38.048°, 44.1°, 64.3°, and 77.3° corresponding to (111), (200), (220), and (311) planes of silver were reported in the standard powder diffraction card of JCPDS, silver file No. 04-0783. Because of low amount, high distribution, and small crystallite size of Ag particles, we did not detect the main diffractions of metallic Ag in XRD pattern of the quaternary TFC-Ag(a) nanocomposite [43]. Considering XRD patterns (Figs. 2(c)–(e)), we did not observe the major diffraction of MWCNTs at 2θ = 25.5° [40], which was overlapped with the major diffraction of anatase TiO_2 at

2θ = 25.3°. Besides, a relatively large difference between the mass percentage of MWCNTs and TiO_2 and low crystallinity of MWCNTs could be the reasons for the MWCNTs diffraction not to be detectable [44].

We calculated the mean TiO_2 crystal size at 2θ = 25.3° using Scherrer's equation for each sample [45]:

$$D = K\lambda/\beta\cos\theta \quad (1)$$

where D is the sample mean crystal size, λ the X-ray wavelength (1.54056 Å), β the diffraction full width at half maximum (radian), K is a coefficient (0.89), and θ is the diffraction angle at the peak maximum. The TiO_2 crystal sizes in all obtained nanocomposites are within a nanometric size range (Table 1).

The lattice parameters corresponding to tetragonal crystalline structure ($a = b \neq c$) were obtained for (101) crystal plane of anatase phase, by Eq. (2):

$$1/d^2 = (h^2 + k^2)/a^2 + l^2/c^2 \quad (2)$$

Table 1
Phase, crystal size, and lattice parameters of the prepared samples

Sample	Phase	Crystal size (nm)	$a = b$ (Å)	c (Å)	Cell volume (Å^3)
TiO_2	Anatase	6.78	3.76	9.40	132.89
TFC-Ag(2.58)	Anatase	6.94	3.78	9.36	133.73
TFC-Ag(1.79)	Anatase	5.93	3.78	9.30	132.88
TFC-Ag(3.18)	Anatase	6.78	3.78	9.32	133.17

Considering the interplanar spacing (d_{hkl}), the distance between adjacent planes in the set (hkl) can be determined using the Bragg's law:

$$d_{hkl} = \lambda/2\sin\theta \quad (3)$$

The cell volume (tetragonal one) was calculated as follows:

$$V = a^2c \quad (4)$$

where a and c are considered lattice parameters. Table 1 shows the lattice parameters of prepared samples.

The obtained values of the lattice parameters for TiO_2 in the prepared samples matched well with the anatase structure (Joint Committee for Powder Diffraction Standard, 78-2486) of TiO_2. The diffraction peaks and lattice parameters of TiO_2 remained unchanged, confirming that silver atoms does not enter into the TiO_2 framework and loading on the TiO_2 NPs surface and did not change the crystal structure of TiO_2.

3.2. FESEM/EDX and TEM analysis

Fig. 3 shows the field emission scanning electron microscopy (FESEM) images of TFC and TFC-Ag(a) nanocomposites. These images show that TiO_2 NPs attach to the MWCNTs surface and exhibit the decoration surface of TiO_2 and MWCNTs by metallic silver NPs. The EDX results were applied to evaluate elemental composition of TFC and TFC-Ag(a) nanocomposites (Fig. 4 and Table 2). Our obtained EDX analysis data verify the presence of C, Ti, O,

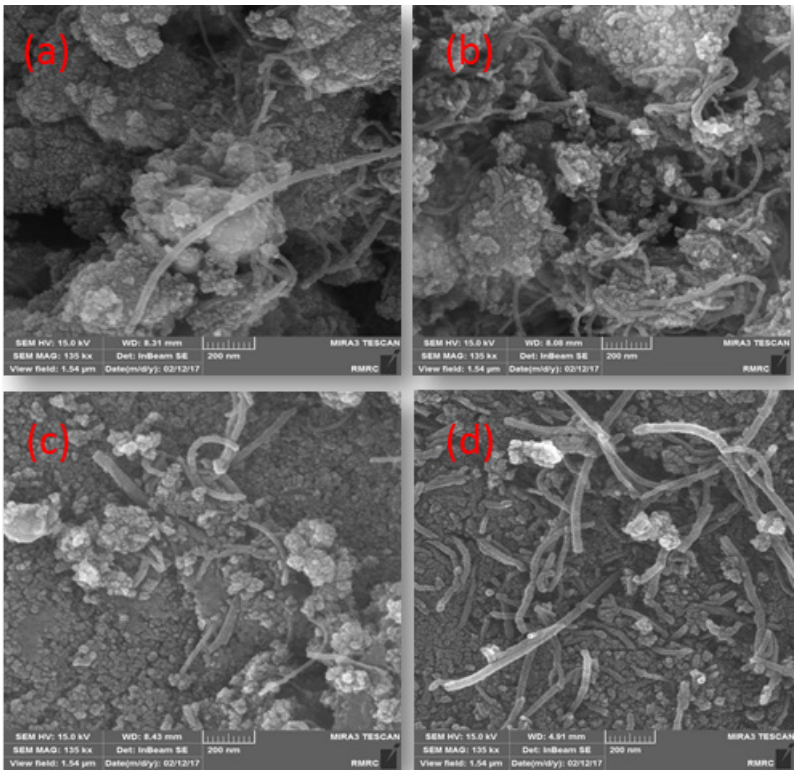

Fig. 3. FESEM images of (a) TFC-Ag(2.58), (b) TFC-Ag(1.79), (c) TFC-Ag(3.18), and (d) TFC.

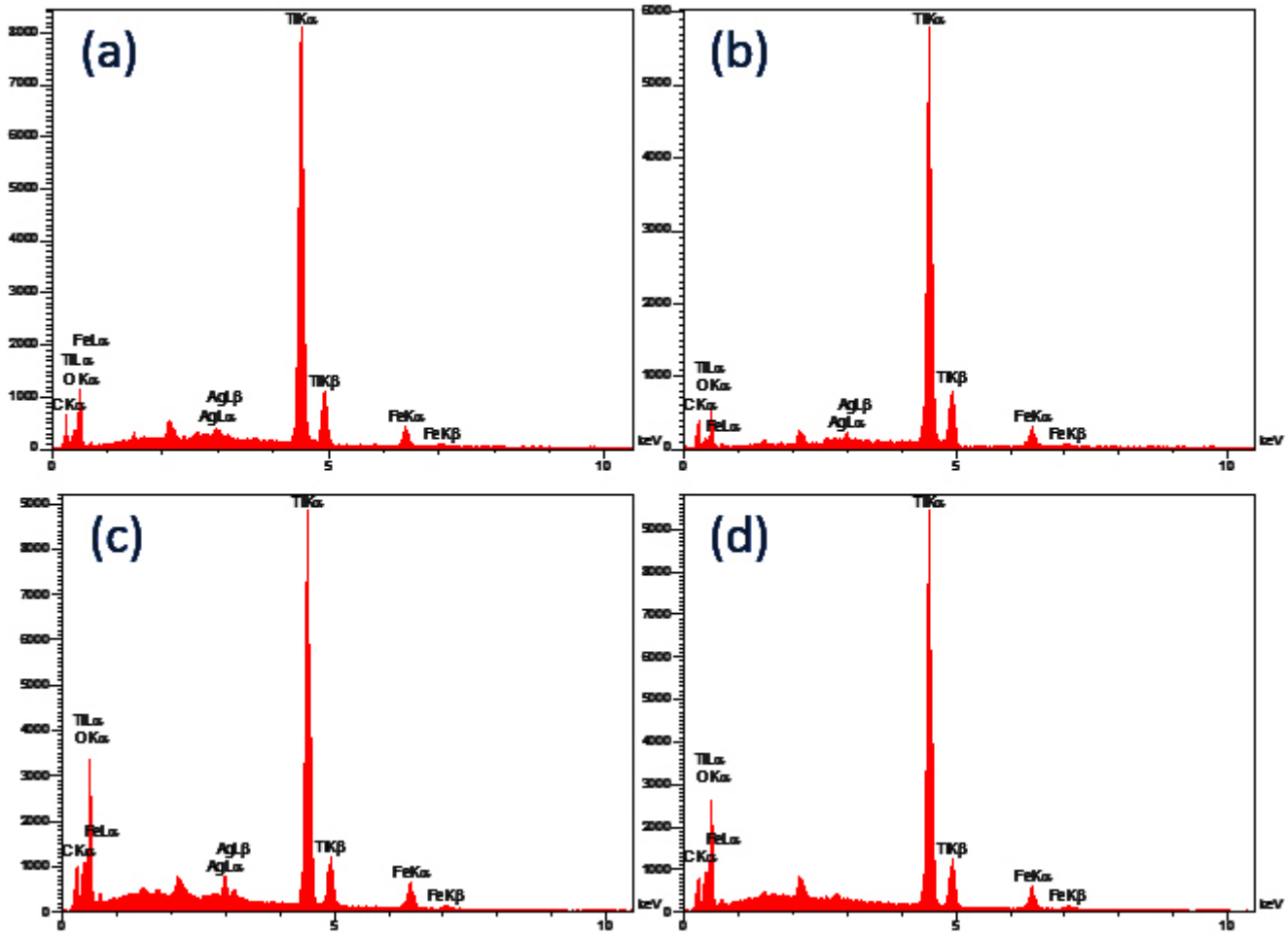

Fig. 4. EDX spectra of (a) TFC-Ag(2.58), (b) TFC-Ag(1.79), (c) TFC-Ag(3.18), and (d) TFC.

Table 2
Elemental chemical analysis of the prepared samples

Sample	C (wt%)	O (wt%)	Ti (wt%)	Fe (wt%)	Ag (wt%)
TFC	9.61	41.60	43.40	5.40	0.00
TFC-Ag(2.58)	9.53	26.22	56.08	5.59	2.58
TFC-Ag(1.79)	10.63	20.39	60.52	6.67	1.79
TFC-Ag(3.18)	11.06	41.66	38.38	5.73	3.18

Fe, and Ag elements in the prepared samples. In the EDX spectra of TFC-Ag(a) samples, the absorption peak at 3 keV can be indexed to metallic silver in the prepared samples [46]. Elemental mapping (Fig. 5) shows that C, Ti, O, Fe, and Ag elements are dispersed uniformly over the testing area, indicating the uniform distribution of TiO_2 and Ag NPs over the surface of MWCNTs.

Fig. 6 shows a TEM image of our optimum photocatalyst in this work (TFC-Ag(1.79) nanocomposite). According to these images, TiO_2 NPs are uniformly dispersed on the wall of MWCNTs and Ag NPs are loaded on the TiO_2 NPs and MWCNTs surface.

3.3. DRS analysis

DRS studies contribute to perceive the material band gaps. During the photoreaction, the band gaps would alter as the catalysts would be exposed to photons of various energies [47]. Fig. 7(a) demonstrates the pure TiO_2, TFC, and TFC-Ag(a) samples diffuse reflectance spectra over the 200–800 nm wavelength range. There is a broad intense absorption around 400 nm in the DR spectrum of pure TiO_2 because of the charge-transfer from the valence band formed by 2p orbitals of the oxide anions to the conduction band formed by 3d t_{2g} orbitals of the Ti^{4+} cations [48]. In the DR spectra of TFC-Ag(a) samples, we can observe the absorption shoulder peak in the range between 360 and 500 nm. These absorption shoulders result from the post-broadening SPR peak [49]. In the visible region, the presence of localized surface plasmon resonance (LSPR) would enable the quaternary nanocomposites to show broad and strong absorption [50,51]. The absorption tail of these samples in the range of 500–800 nm remained unchanged. Therefore, it is inferred that the MWCNTs remained active and played their crucial role in capturing photoexcited electrons after decoration with TiO_2 and Ag. This similar characteristic of the absorption tail was also reported in other MWCNTs-based photocatalysts [52]. We also calculated the band gap energy from

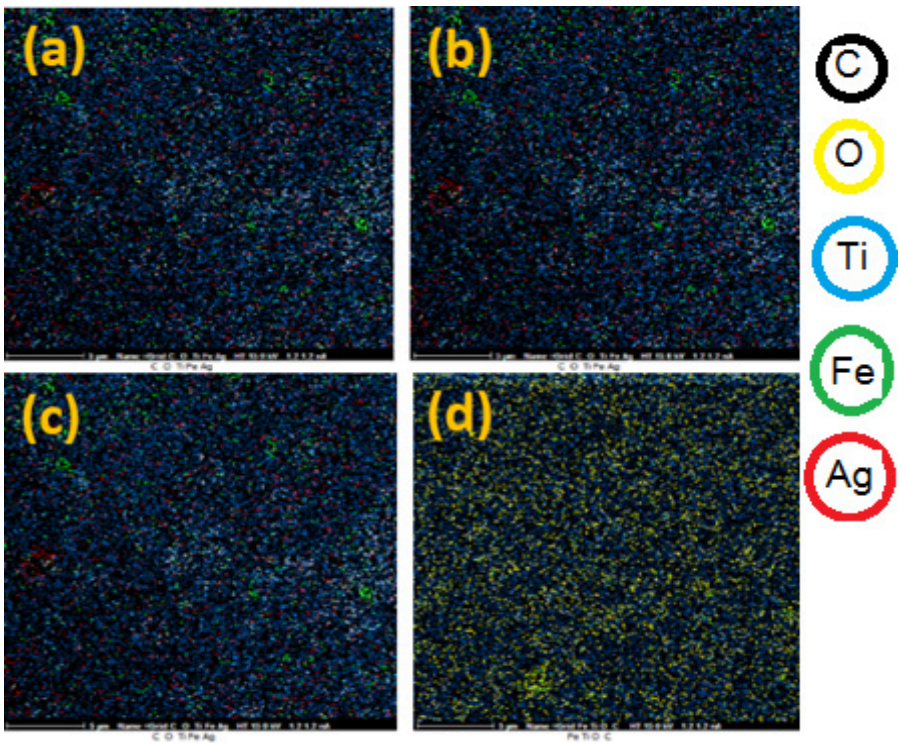

Fig. 5. Elemental mapping of (a) TFC-Ag(2.58), (b) TFC-Ag(1.79), (c) TFC-Ag(3.18), and (d) TFC.

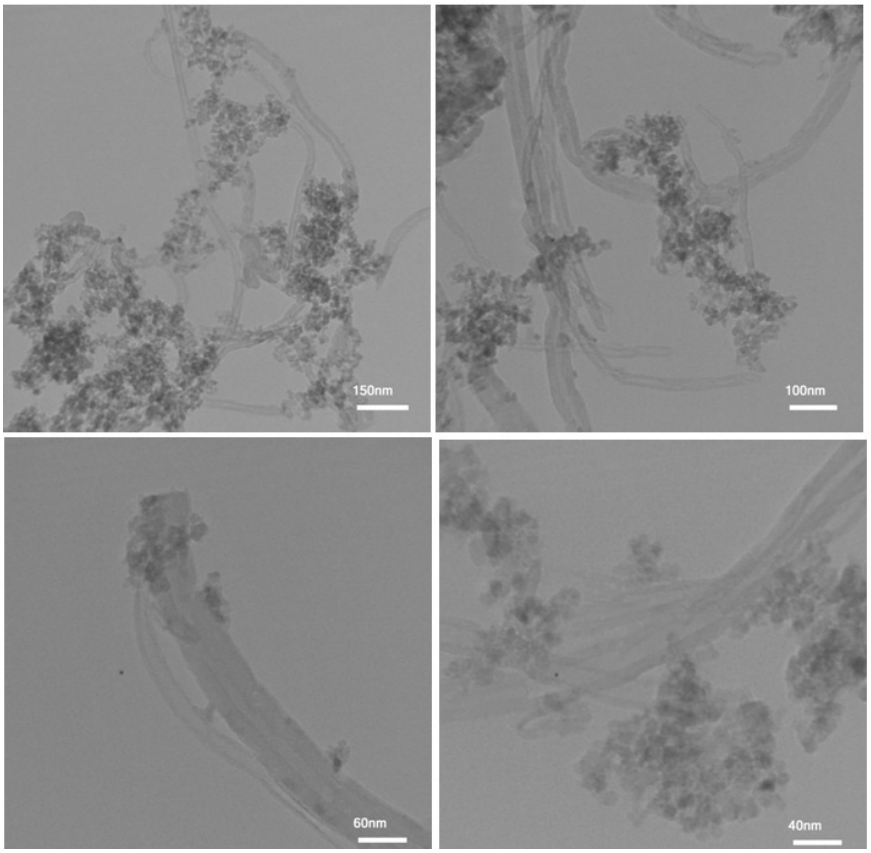

Fig. 6. TEM image of TFC-Ag(1.79) nanocomposite at various magnifications.

the DR spectra according to Eq. (5) [53] for the synthesized samples.

$$[F(R)h\upsilon]^{0.5} = A(h\upsilon - E_g) \quad (5)$$

where A is a constant, $F(R)$ is the function of Kubelka–Munk, and E_g is the band gap. The E_g data of samples are presented in Table 3. The TFC-Ag(a) samples band gap decreased slightly compared with TiO_2 (Table 3). It can be clearly seen that Ag NPs loaded on the TiO_2 surface affect the TiO_2 optical properties significantly. Evidently, the photoresponse of the TFC-Ag(a) nanocomposite is greatly shifted into the visible light ranges because of the SPR properties of metallic silver NPs, leading to a band gap narrowing (2.62 eV) compared with that of pure TiO_2 (2.95 eV).

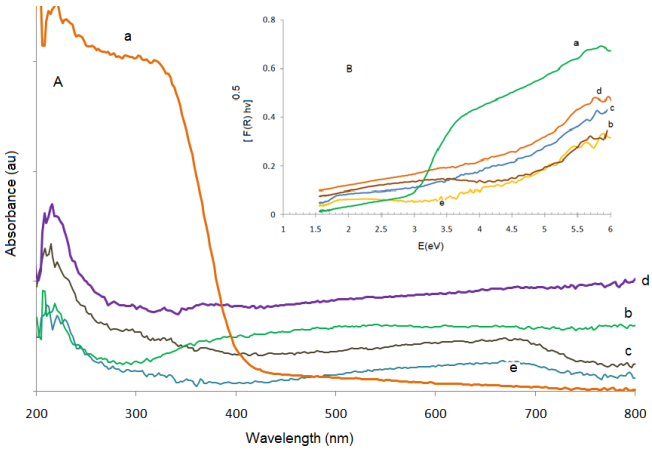

Fig. 7. (A) Diffuse reflectance spectra and (B) Kubelka–Munk plots for the band gap energy calculation of (a) TiO_2, (b) TFC, (c) TFC-Ag(2.58), (d) TFC-Ag(1.79), and (e) TFC-Ag(3.18).

3.4. N_2 physisorption analysis

Fig. 8 illustrates the N_2 adsorption–desorption isotherms carried out in the present work. The sorption isotherms for all the prepared samples correspond to the type IV isotherm according to the IUPAC classification [54]. Textural and structural parameters of the obtained samples are shown in Table 4.

Table 3
Band gap energy of the prepared samples

Sample	E_g (eV)
TiO_2	2.95
TFC	2.80
TFC-Ag(2.58)	2.75
TFC-Ag(1.79)	2.62
TFC-Ag(3.18)	2.92

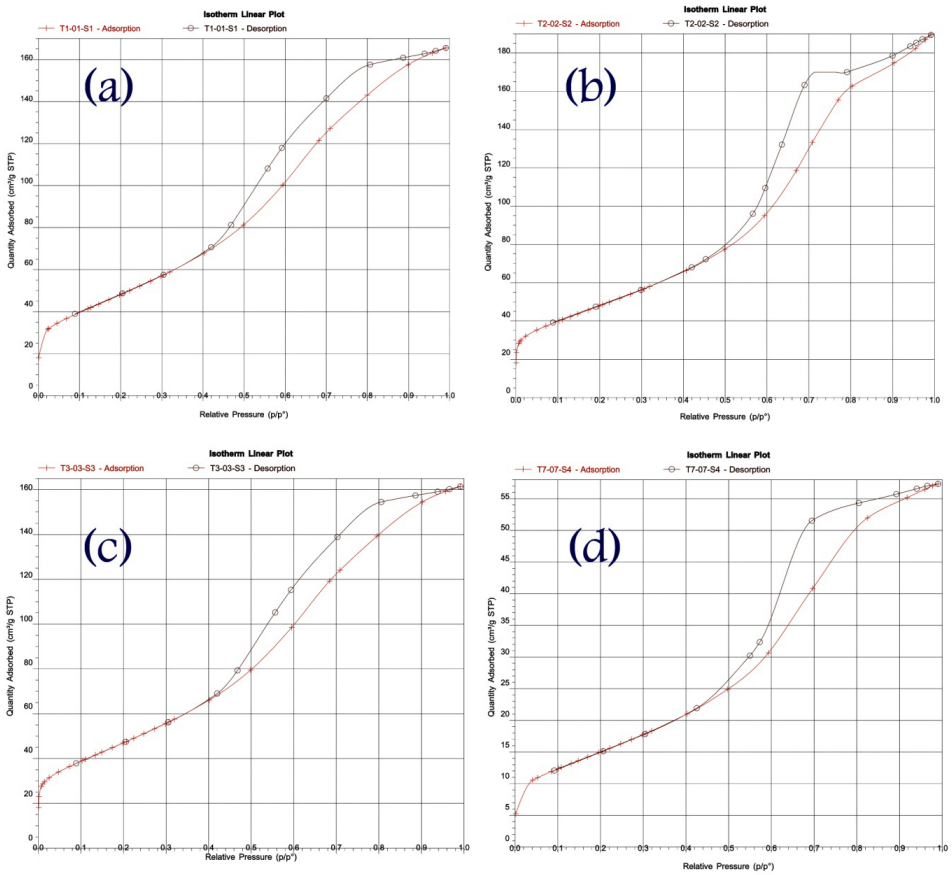

Fig. 8. N_2 adsorption–desorption isotherms for (a) TFC-Ag(2.58), (b) TFC-Ag(1.79), (c) TFC-Ag(3.18), and (d) TFC.

Specific surface areas and average pore diameter were calculated according to the BET method, where pore volumes were derived from the desorption branch according to the Barrett–Joyner–Halenda model. The results show that the BET surface area of quaternary nanocomposites (TFC-Ag samples) is larger than the starting material (TFC sample), indicating the loading of Ag NPs on the surface of TFC ternary nanocomposite.

3.5. Magnetic properties of the nanocomposites

The saturation magnetization (M_s) of the samples was measured to study the magnetic reaction of the magnetic nanocomposites to an external field. According to Fig. 9, the photocatalysts are superparamagnetic at room temperature [55]. It is worth noting that the M_s value of the Fe_3O_4 NPs is significantly higher than that of TFC and TFC-Ag(a) samples, which is because the Fe_3O_4 NPs are covered with an anatase TiO_2 layer in the TFC and TFC-Ag(a) samples. The small decrease in M_s value of the TFC-Ag(a) samples in comparison with that of the TFC sample (Fig. 9) can be explained by the slight increase in mass and size owing to the adherence of Ag NPs to the surface of magnetic composites. Furthermore, no significant variation was seen in the coercivity. Such excellent magnetic properties imply a strong magnetic responsivity on the samples, enabling them to be recycled easily from solution through an external magnetic force. Also, the simple rapid separation and redispersion of the TFC-Ag(a) samples can be recognized.

Table 4
Textural and structural parameters of the prepared sample

Sample	S_{BET} (m^2/g)	Average pore diameter (nm)	Pore volume (cm^3/g)
TFC-Ag(2.58)	180.60	5.60	0.27
TFC-Ag(1.79)	177.33	6.45	0.30
TFC-Ag(3.18)	176.38	5.60	0.26
TFC	56.06	6.28	0.09

3.6. Photocatalytic activity evaluation

The synthesized samples photoactivity performance were investigated for the aqueous solution photocatalytic degradation of 2,4-DCP as a model of organic pollutant (Figs. 10 and 11). Under visible light, the quaternary

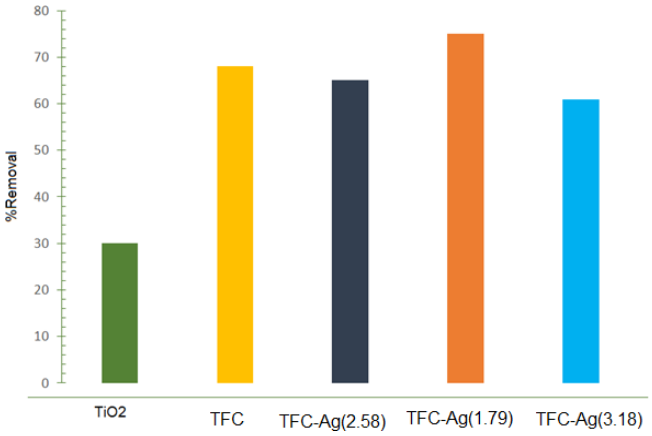

Fig. 10. Photocatalytic degradation of 2,4-DCP in the presence of the prepared samples under visible light (Initial concentration of 2,4-DCP, 40 mg/L; volume, 100 mL; catalyst dosage, 10 mg, 180 min irradiation).

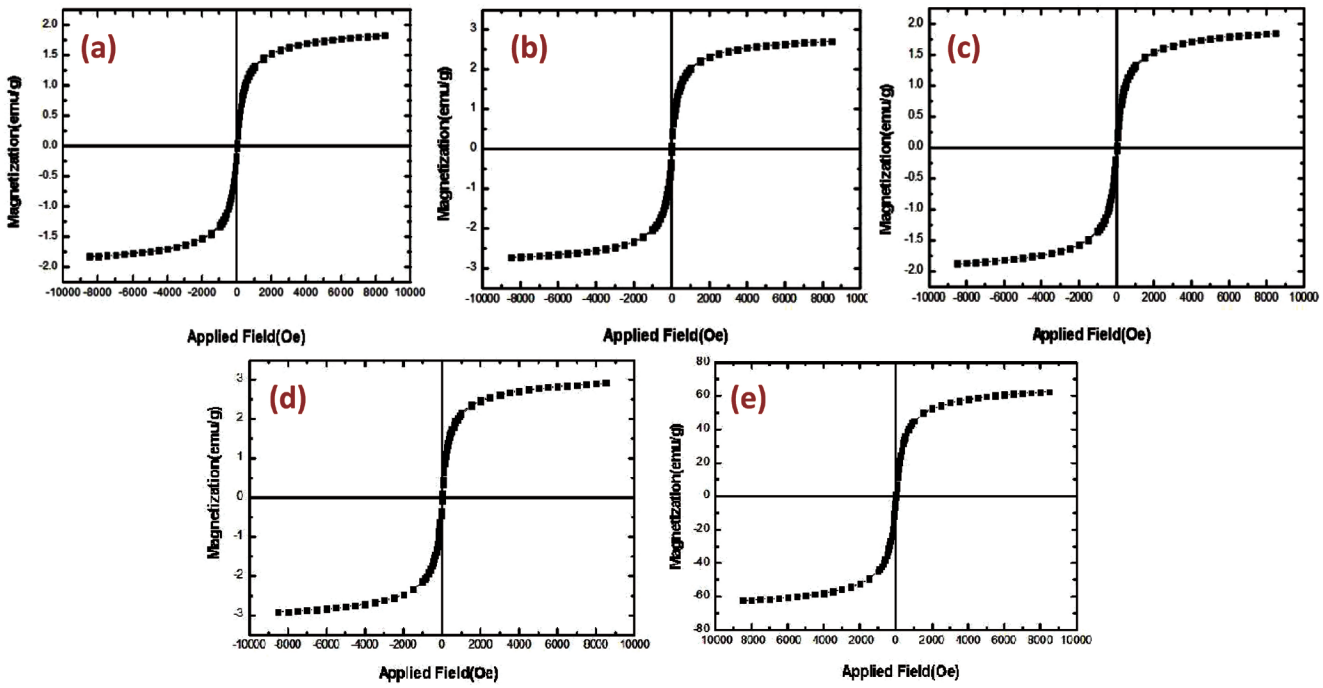

Fig. 9. Comparison of hysteresis curves of (a) TFC-Ag(2.58), (b) TFC-Ag(1.79), (c) TFC-Ag(3.18), (d) TFC, and (e) Fe_3O_4.

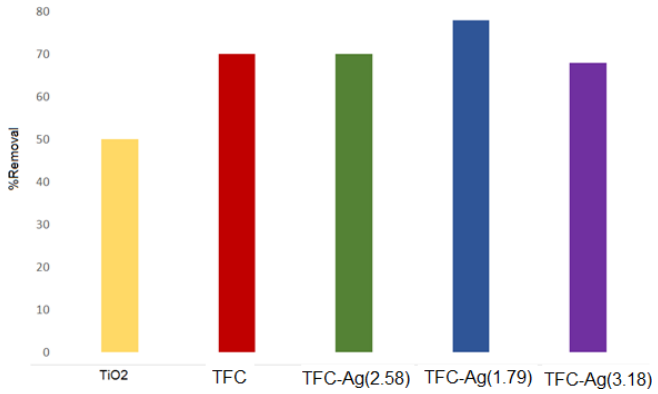

Fig. 11. Photocatalytic degradation of 2,4-DCP in the presence of the prepared samples under UV irradiation (Initial concentration of 2,4-DCP, 40 mg/L; volume, 100 mL; catalyst dosage, 10 mg, 180 min irradiation).

photocatalyst with 1.75 wt% of Ag (TFC-Ag(1.75) sample) showed the highest performance for 2,4-DCP photocatalytic degradation, that is, 75% after 180 min irradiation. This enhancement in photoactivity of quaternary nanocomposite can be attributed to the plasmonic influence of Ag NPs and MWCNTs can act as electron reservoir. Under UV irradiation, pure TiO_2 and other photocatalysts showed a higher photoactivity compared with their activity under visible light due to the higher photoenergy of UV irradiation than visible light. The quaternary photocatalysts with the higher loading of silver content showed a lower photocatalytic performance of 2,4-DCP degradation under visible and UV irradiation. The higher silver loading has shading effect and blocked the light reaching with the TiO_2 surface, resulting in a lower photocatalytic performance [56,57]. The higher photocatalytic efficiency of quaternary TFC-Ag(a) nanocomposites compared with the other photocatalysts in this work can be explained by the SPR influence of Ag NPs and the lower band gap of the quaternary nanocomposite. In quaternary nanocomposites, high-energy electrons were generated because of LSPR of metallic silver NPs under visible light. Fig. 12 shows our proposed mechanism for photocatalytic degradation of 2,4-DCP over TFC-Ag(1.79) sample under visible light. These generated electrons are transferred and excited from Ag NPs to the conduction band of TiO_2. As a result, the generated holes remain on the Ag NPs and oxidize the organic target [58]. Also, due to the higher work function of MWCNTs than TiO_2 semiconductor, the electrons transfer from TiO_2 to MWCNTs and the recombination rate suppressed and the quaternary photocatalysts showed a higher photocatalytic activity [59]. The adsorbed oxygen molecules on the TiO_2 surface trapped the electron from the conduction band of TiO_2, leading to the generation of some active species such as $OH^•$ and $O_2^{•-}$ radicals. These active species attack the 2,4-DCP molecules and decompose them. Due to the heterojunctions formation, there are many defects in TiO_2 that decrease the energy of conduction band of TiO_2 [60] in quaternary nanocomposite and TiO_2 can absorb visible light and generate electrons and holes under visible light. These charge carriers can participate in the destruction of 2,4-DCP under visible light and produce more oxygen active species such as $OH^•$ and $O_2^{•-}$ radicals. In this way, the photocatalytic

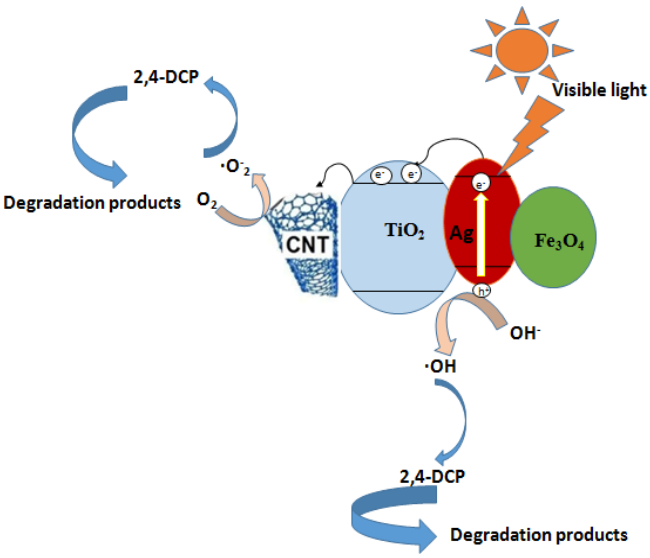

Fig. 12. Our proposed mechanism for photocatalytic degradation of 2,4-DCP over TFC-Ag(1.79) sample under visible light.

activity enhances due to more charge carrier generation. Under UV irradiation, photogenerated electrons from the valence band of TiO_2 can transfer to the conduction band of TiO_2 and thus the holes remain in the valence band of TiO_2. In the next step, because of the work function difference of TiO_2 and Ag and the Schottky barrier formation at Ag/TiO_2 interface, the electrons transferred from TiO_2 to Ag NPs. This transition can reduce the recombination rate of the electron–hole pair [61]. Also, because of the higher work function of MWCNTs compared with TiO_2, the photogenerated electrons on theTiO_2 surface can be absorbed by MWCNTs and the rate of electron–hole recombination can be decreased. Accordingly, the electrons can react with oxygen molecules and generate some active oxygen species such as superoxide radicals ($O_2^{•-}$) and $OH^•$ radicals and the remained holes can react with the H_2O molecules and produce OH radicals. These active species are the main species responsible for 2,4-DCP degradation and the quaternary nanocomposites display a better photocatalytic activity than the ternary nanocomposite and pure TiO_2.

3.7. Kinetic study

The kinetic parameters for the elimination of 2,4-DCP are shown in Table 5. Obtained results show the reaction is the first-order type with its kinetics expressed as $\ln(C_0/C) = k_{obs}t$. In this equation, k_{obs} (min^{-1}) is the constant of apparent rate, C_0 and C are the initial concentration and concentration of 2,4-DCP at reaction time t. The initial reaction rate of 2,4-DCP photocatalytic degradation is faster at higher initial concentration and the rate constants decrease by increasing the initial concentrations of 2,4-DCP. This result can be explained by the short lifetime of active species formed during the reaction. The active oxygen species such as $OH^•$ and $O_2^{•-}$ are formed on the surface of TFC-Ag(1.75). However, they could not go far away and react with the 2,4-DCP molecules near the photocatalyst surface. Thus, the initial degradation rate is faster at high initial concentrations of 2,4-DCP.

Table 5
Kinetic parameters for degradation of 2,4-DCP over TFC-Ag(1.75)

Concentration (mg/L)	R^2	Initial reaction rate (mg/L.(min^{-1}))	k_{obs} (min^{-1})	$t_{1/2}$ (min)
10	0.9981	0.0771	0.0077	90.0200
20	0.9980	0.1162	0.0058	119.4827
30	0.9984	0.1711	0.0057	121.5789
40	0.9988	0.2082	0.0052	133.2692

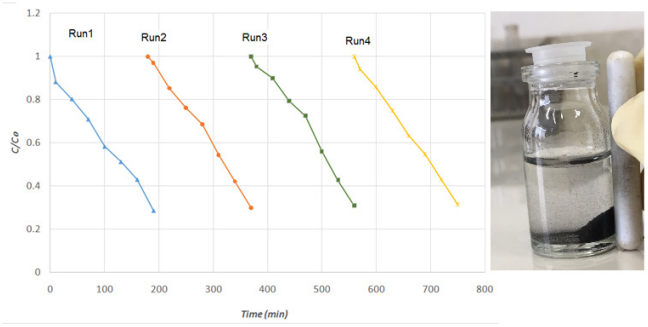

Fig. 13. Recyclability of the TFC-Ag(1.79) for photocatalytic degradation of 2,4-DCP after four successive cycles (catalyst dose: 0.1 g/L; [2,4-DCP]: 40 mg/L).

3.8. Recyclability of TFC-Ag(1.75) photocatalyst

The recyclability of photocatalysts is one vital importance for developing heterogeneous photocatalysis process for wastewater treatment and can contribute significantly to reducing the operational cost. The recyclability of the TFC-Ag(1.75) quaternary nanocomposite was examined by applying the same 2,4-DCP photocatalytic degradation in four repeated cycles. The photocatalytic degradation of 2,4-DCP remains unchanged during the first four cycles (Fig. 13). These obtained results indicated that the removal of the photocatalyst was effective because of magnetic Fe_3O_4 NPs; thus, the TFC-Ag(1.75) photocatalyst was recyclable and promising for practical applications.

4. Conclusion

In summary, visible-light-driven quaternary TiO_2/Fe_3O_4/MWCNTs/Ag photocatalysts including various amounts of silver were prepared by a facile method. The obtained photocatalysts were characterized by different analysis techniques such as XRD, DRS, N_2 physisorption, TEM, and SEM/EDX. The prepared samples exhibited a high adsorption capacity and an excellent visible light photocatalytic activity for degradation of 2,4-DCP as an organic pollutant model. The high photocatalytic activity can be attributed to both the high photocatalyst specific surface areas and the plasmon resonance of silver NPs. Therefore, the high adsorption capacity and effective photocatalytic efficiency of the prepared quaternary TiO_2/Fe_3O_4/MWCNTs/Ag nanocomposites make them suitable photocatalyst for environmental applications. The degradation reactions followed the first-order kinetics. Reusing experiments of the optimum photocatalyst (TFC-Ag(1.75)) did not reveal any reduction in catalyst activity for degradation of 2,4-DCP under visible light after four cycles.

Acknowledgments

The authors wish to acknowledge the financial support of University of Tehran for supporting of this research. Also, they wish to acknowledge the financial support of Iran Nanotechnology Initiative Council (INIC) Foundation (Grant No: 120345).

References

[1] C.-T. Dinh, H. Yen, F. Kleitz, T.-O. Do, Three-dimensional ordered assembly of thin-shell Au/TiO_2 hollow nanospheres for enhanced visible-light-driven photocatalysis, Angew. Chem. Int. Ed., 53 (2014) 6618–6623.
[2] J. Schneider, M. Matsuoka, M. Takeuchi, J. Zhang, Y. Horiuchi, M. Anpo, D.W. Bahnemann, Understanding TiO_2 photocatalysis mechanisms and materials, Chem. Rev., 114 (2014) 9919–9986.
[3] Z. Lu, P. Huo, Y. Luo, X. Liu, Y. Yan, Performance of molecularly imprinted photocatalysts based on fly-ash cenospheres for selective photodegradation of single and ternary antibiotics solution, J. Mol. Catal. A: Chem., 378 (2013) 91–98.
[4] A. Bansal, S. Madhavi, T.T.Y. Tan, Effect of silver on the photocatalytic degradation of humic acid, Catal. Today, 131 (2008) 250–254.
[5] J. Kim, J. Lee, W. Choi, Urgent high quality communications from across the chemical sciences, Chem. Commun., 5 (2008) 756.
[6] A. Shafaei, M. Nikazar, M. Arami, Photocatalytic degradation of terephthalic acid using titania and zinc oxide photocatalysts: comparative study, Desalination, 252 (2010) 8–16.
[7] X. Cheng, X. Yu, Z. Xing, Characterization and mechanism analysis of N doped TiO_2 with visible light response and its enhanced visible activity, Appl. Surf. Sci., 258 (2012) 3244–3248.
[8] Z. Lu, F. Chen, M. He, M. Song, P. Xiao, Microwave synthesis of a novel magnetic imprinted TiO_2 photocatalyst with excellent transparency for selective photodegradation of enrofloxacin hydrochloride residues solution, Chem. Eng. J., 249 (2014) 15–26.
[9] Z. Jiang, D. Liu, D. Jiang, W. Wei, K. Qian, M. Chen, Bamboo leaf-assisted formation of carbon/nitrogen co-doped anatase TiO_2 modified with silver and graphitic carbon nitride novel and green synthesis and cooperative photocatalytic activity, J. Chem. Soc., Dalton Trans., 43 (2014) 13792–13802.
[10] R.R. Bhosale, S.R. Pujari, M.K. Lande, Photocatalytic activity and characterization of sol–gel-derived Ni-doped TiO_2-coated active carbon composites, Appl. Surf. Sci., 261 (2012) 835–841.
[11] J. Lukac, M. Klementova, P. Bezdicka, S. Bakardjieva, J. Subrt, L. Szatmary, Influence of Zr as TiO_2 doping ion on photocatalytic degradation of 4-chlorophenol, Appl. Catal., B, 74 (2007) 83–91.
[12] M. Asilturk, F. Sayilkan, E. Arpac, Effect of Fe^{3+} ion doping to TiO_2 on the photocatalytic degradation of Malachite Green dye under UV and vis irradiation, J. Photochem. Photobiol., A, 203 (2009) 64–71.
[13] S. Rehman, R. Ullah, A.M. Butt, N.D. Gohar, Strategies of making TiO_2 and ZnO visible light active, J. Hazard. Mater., 170 (2009) 560–569.
[14] B. Abdollahi Nejand, S. Sanjabi, V. Ahmadi, Sputter deposition of high transparent $TiO_{2-x}N_x/TiO_2$/ZnO layers on glass for development of photocatalytic self-cleaning application, Appl. Surf. Sci., 257 (2011) 10434–10442.
[15] K.K. Akurati, A. Vital, J.P. Dellemann, K. Michalow, T. Graule, D. Fetti, Flame made WO_3/TiO_2 nanoparticles relation between surface acidity, structure and photocatalytic activity, Appl. Catal., B, 79 (2008) 53–62.

[16] M. Pirhashemi, A. Habibi-Yangjeh, Ultrasonic-assisted preparation of plasmonic ZnO/Ag/Ag_2WO_4 nanocomposites with high visible-light photocatalytic performance for degradation of organic pollutants, J. Colloid Interface Sci., 491 (2017) 216–229.
[17] A. Akhundi, A. Habibi-Yangjeh, High performance magnetically recoverable g-C_3N_4/Fe_3O_4/Ag/Ag_2SO_3 plasmonic photocatalyst for enhanced photocatalytic degradation of water pollutants, Adv. Powder Technol., 28 (2017) 565–574.
[18] S. Naghizadeh-Alamdari, A. Habibi-Yangjeh, M. Pirhashemi, One-pot ultrasonic-assisted method for preparation of Ag/AgCl sensitized ZnO nanostructures as visible-light-driven photocatalysts, Solid State Sci., 40 (2015) 111–120.
[19] Z. Xuming, C. Yu Lim, L. Ru-Shi, T. Din Ping, Plasmonic photocatalysis, Rep. Prog. Phys., 76 (2013) 046401.
[20] S. Linic, P. Christopher, D.B. Ingram, Plasmonic-metal nanostructures for efficient conversion of solar to chemical energy, Nat. Mater., 10 (2011) 911–921.
[21] J. Lee, S. Mubeen, X. Ji, G.D. Stucky, M. Moskovits, Plasmonic photoanodes for solar water splitting with visible light, Nano Lett., 12 (2012) 5014–5019.
[22] V.R. Djokić, A.D. Marinković, M. Mitrić, P.S. Uskoković, R.D. Petrović, V.R. Radmilović, D.T. Janaćković, Preparation of TiO_2/carbon nanotubes photocatalysts the influence of the method of oxidation of the carbon nanotubes on the photocatalytic activity of the nanocomposites, Ceram. Int., 38 (2012) 6123–6129.
[23] R. Leary, A. Westwood, Carbonaceous nanomaterials for the enhancement of TiO_2 photocatalysis, Carbon, 49 (2011) 741–772.
[24] S. DaDalt, A.K. Alves, C.P. Bergmann, Photocatalytic degradation of methyl orange dye in water solutions in the presence of MWCNT/TiO_2 composites, Mater. Res. Bull., 48 (2013) 1845–1850.
[25] Z. Peining, A.S. Nair, Y. Shengyuan, S. Ramakrishna, TiO_2–MWCNT rice grain-shaped nanocomposites: synthesis, characterization and photocatalysis, Mater. Res. Bull., 46 (2011) 588–595.
[26] C. Liu, H. Chen, K. Dai, A. Xue, H. Chen, Q. Huang, Synthesis, characterization, and its photocatalytic activity of double-walled carbon nanotubes-TiO_2 hybrid, Mater. Res. Bull., 48 (2013) 1499–1505.
[27] A. Habibi-Yangjeh, M. Shekofteh-Gohari, Novel magnetic Fe_3O_4/ZnO/$NiWO_4$ nanocomposites: enhanced visible-light photocatalytic performance through p-n heterojunctions, Sep. Purif. Technol., 184 (2017) 334–346.
[28] M. Shekofteh-Gohari, A. Habibi-Yangjeh, Fe_3O_4/ZnO/$CoWO_4$ nanocomposites: novel magnetically separable visible-light-driven photocatalysts with enhanced activity in degradation of different dye pollutants, Ceram. Int., 43 (2017) 3063–3071.
[29] M. Mousavi, A. Habibi-Yangjeh, M. Abitorabi, Fabrication of novel magnetically separable nanocomposites using graphitic carbon nitride, silver phosphate and silver chloride and their applications in photocatalytic removal of different pollutants using visible-light irradiation, J. Colloid Interface Sci., 480 (2016) 218–231.
[30] M. Mousavi, A. Habibi-Yangjeh, Magnetically separable ternary g-C_3N_4/Fe_3O_4/BiOI nanocomposites: novel visible-light-driven photocatalysts based on graphitic carbon nitride, J. Colloid Interface Sci., 465 (2016) 83–92.
[31] M. Mousavi, A. Habibi-Yangjeh, Novel magnetically separable g-C_3N_4/Fe_3O_4/Ag_3PO_4/Co_3O_4 nanocomposites: visible-light-driven photocatalysts with highly enhanced activity, Adv. Powder Technol., 28 (2017) 1540–1553.
[32] Z. Lu, X. Zhao, Z. Zhu, Y. Yan, W. Shi, H. Dong, Z. Ma, N. Gao, Y. Wang, H. Huang, Enhanced recyclability, stability and selectivity of CdS/C@Fe_3O_4 nanoreactors for orientation photodegradation of ciprofloxacin, Chem. Eur. J., 21 (2015) 18528–18533.
[33] U.G. Ahlborg, T.M. Thunberg, Chlorinated phenols: occurrence, toxicity, metabolism, and environmental impact, Crit. Rev. Toxicol., 7 (1980) 1–35.
[34] H.C. Lee, J.H. In, J.H. Kim, K.Y. Hwang, C.H. Lee, Kinetic analysis for decomposition of 2,4-dichlorophenol by supercritical water oxidation, Korean J. Chem. Eng., 22 (2005) 882–888.
[35] D.D. Dionysiou, A.P. Khodadoust, A.M. Kern, M.T. Suidan, I. Baudin, J.-M., Laîné, Continuous-mode photocatalytic degradation of chlorinated phenols and pesticides in water using a bench-scale TiO_2 rotating disk reactor, Appl. Catal., B, 24 (2000) 139–155.
[36] K. Arnoldsson, P.L. Andersson, P. Haglund, Formation of environmentally relevant brominated dioxins from 2,4,6,-tribromophenol via bromoperoxidase-catalyzed dimerization, Environ. Sci. Technol., 46 (2012) 7239–7244.
[37] J. Bandara, J.A. Mielczarski, A. Lopez, J. Kiwi, Sensitized degradation of chlorophenols on iron oxides induced by visible light comparison with titanium oxide, Appl. Catal., B, 34 (2001) 321–333.
[38] S. Laurent, D. Forge, M. Port, A. Roch, C. Robic, L. Vander Elst, R.N. Muller, Magnetic iron oxide nanoparticles: synthesis, stabilization, vectorization, physicochemical characterizations, and biological applications, Chem. Rev., 108 (2008) 2064–2110.
[39] C.A. Huerta Aguilar, T. Pandiyan, J.A. Arenas-Alatorre, N. Singh, Oxidation of phenols by TiO_2AFe_3O_4AM (M = Ag or Au) hybrid composites under visible light, Sep. Purif. Technol., 149 (2015) 265–278.
[40] B. Ahmmad, Y. Kusumoto, S. Somekawa, M. Ikeda, Carbon nanotubes synergistically enhance photocatalytic activity of TiO_2, Catal. Commun., 9 (2008) 1410–1413.
[41] Z. Mo, C. Zhang, R. Guo, S. Meng, J. Zhang, Synthesis of Fe_3O_4 nanoparticles using controlled ammonia vapor diffusion under ultrasonic irradiation, ◎Ind. Eng. Chem. Res., 50 (2011) 3534–3539.
[42] J. Lu, M. Wang, C. Deng, X. Zhang, Facile synthesis of Fe_3O_4@mesoporous TiO_2 microspheres for selective enrichment of phosphopeptides for phosphoproteomics analysis, Talanta, 105 (2013) 20–27.
[43] L. Yinghua, W. Huan, L. Li, C. Wenquan, Facile synthesis of Ag@AgCl plasmonic photocatalyst and its photocatalytic degradation under visible light, Rare Met. Mater. Eng., 44 (2015) 1088–1093.
[44] W. Wang, P. Serp, P. Kalck, Visible light photodegradation of phenol on MWNT-TiO_2 composite catalysts prepared by a modified sol–gel method, J. Mol. Catal. A: Chem., 235 (2005) 194–199.
[45] M. Khan, W. Cao, Cationic (V, Y)-codoped TiO_2 with enhanced visible light induced photocatalytic activity a combined experimental, theoretical study, J. Appl. Phys., 114 (2013) 183514.
[46] S. Kaviya, J. Santhanalakshmi, B. Viswanathan, J. Muthumar, K. Srinivasan, Biosynthesis of silver nanoparticles using citrus sinensis peel extract and its antibacterial activity, Spectrochim. Acta, Part A, 79 (2011) 594–598.
[47] G. Sadanandam, K. Lalitha, V.D. Kumari, M.V. Shankar, M. Subrahmanyama, Cobalt doped TiO_2: a stable and efficient photocatalyst for continuous hydrogen production from glycerol: water mixtures under solar light irradiation, Int. J. Hydrogen Energy, 38 (2013) 9655–9664.
[48] M. Hamadanian, A. Reisi-Vanani, A. Majedi, Sol-gel preparation and characterization of Co/TiO_2 nanoparticles application to the degradation of methyl orange, J. Iran. Chem. Soc., 7 (2010) 52–58.
[49] Y. Koo, G. Littlejohn, B. Collins, Y. Yun, V.N. Shanov, M. Schulz, D. Pai, J. Sankar, Synthesis and characterization of Ag–TiO_2-CNT nanoparticle composites with high photocatalytic activity under artificial light, Composites Part B, 57 (2014) 105–111.
[50] M.S. ArifSher Shah, K. Zhang, A.R. Park, K.S. Kim, N.-G. Park, J.H. Park, P.J. Yoo, Single-step solvothermal synthesis of mesoporous Ag–TiO_2-reduced graphene oxide ternary composites with enhanced photocatalytic activity, Nanoscale, 5 (2013) 5093–5101.
[51] X. Zhou, G. Liu, J. Yu, W. Fan, Surface plasmon resonance-mediated photocatalysis by noble metal-based composites under visible light, J. Mater. Chem., 22 (2012) 21337–21354.
[52] M.J. Sampaio, C.G. Silva, R.R.N. Marques, A.M.T. Silva, J.L. Faria, Carbon nanotube-TiO_2 thin films for photocatalytic applications, Catal. Today, 161 (2011) 91–96.

[53] S. Kumar, S. Khanchandani, M. Thirumal, A.K. Ganguli, Achieving enhanced visible-light-driven photocatalysis using type-II $NaNbO_3$/CdS core/shell heterostructures, ACS Appl. Mater. Interfaces, 6 (2014) 13221–13233.
[54] K.S.W. Sing, D.H. Everett, R.A.W. Haul, L. Moscou, R.A. Pierotti, Reporting physisorption data for gas/solid systems with special reference to the determination of surface area and porosity, Pure Appl. Chem., 57 (1985) 603–619.
[55] Z. Teng, X. Su, G. Chen, C. Tian, H. Li, L. Ai, G. Lu, Superparamagnetic high-magnetization composite microspheres with Fe_3O_4@SiO_2 core and highly crystallized mesoporous TiO_2 shell, Colloids Surf., A, 402 (2012) 60–65.
[56] K. Kočí, K. Zatloukalová, L. Obalová, S. Krejčíková, Z. Lacný, L. Čapek, A. Hospodková, O. Šolcová, Wavelength effect on photocatalytic reduction of CO_2 by Ag/TiO_2 catalyst, Chin. J. Catal., 32 (2011) 812–815.
[57] X. Yang, T. Xiao, P.P. Edwards, The use of products from CO_2 photoreduction for improvement of hydrogen evolution in water splitting, Int. J. Hydrogen Energy, 36 (2011) 6546–6552.
[58] K.H. Leong, B.L. Gan, S. Ibrahim, P. Saravanan, Synthesis of surface plasmon resonance (SPR) triggered Ag/TiO_2 photocatalyst for degradation of endocrine disturbing compounds, Appl. Surf. Sci., 319 (2014) 128–135.
[59] T. Peng, P. Zeng, D. Ke, X. Liu, X. Zhang, Hydrothermal preparation of multi-walled carbon nanotubes (MWCNTs)/CdS nanocomposite and its efficient photocatalytic hydrogen production under visible light irradiation, Energy Fuels, 25 (2011) 2203–2210.
[60] S.J. Yeo, H. Kang, Y.H. Kim, S. Han, P.J. Yoo, Layer-by-layer assembly of polyelectrolyte multilayers in three-dimensional inverse opal structured templates, ACS Appl. Mater. Interfaces, 4 (2012) 2107–2115.
[61] Y. Wang, L. Liu, L. Xu, C. Meng, W. Zhu, Ag/TiO_2 nanofiber heterostructures highly enhanced photocatalysts under visible light, J. Appl. Phys., 113 (2013) 174311.